Laser-synthesized metastable bismuth nanocrystals chemically bonded to reduced graphene oxide for excellent lithium storage

Su Yanxia[1,2], Zhang Xiuhai[1], Qiu Yuqian[1], Ban Miaohan[1], Zhang Jinbo[1], Li Chong[1,3], Xu Fei[1,*], Wang Hongqiang[1,*]

(1. *State Key Laboratory of Solidification Processing, Centre for Nano Energy Materials, School of Materials Science and Engineering, Northwestern Polytechnical University, Shaanxi Joint Laboratory of Graphene (NPU), Xi'an* 710072, *China*;
2. *Shaanxi Key Laboratory of Surface Engineering and Remanufacturing, Xi'an University, Xi'an* 710065, *China*;
3. *Shaanxi Caihong New Material Co., Ltd, Xianyang* 721000, *China*)

Abstract: The poor interface contact between Bi nanoparticles and reduced graphene oxide (rGO) hinders the transfer of ions/electrons for lithium-ion batteries. We propose an innovative approach for fabricating ultrafine bismuth nanocrystals chemically bonded to reduced graphene oxide (Bi-rGO) by liquid-phase pulsed laser irradiation followed by a solvothermal reaction with graphene oxide. Metastable Bi nanocrystals synthesized by a laser (5.5 nm) are then combined with graphene oxide in a solvothermal process, undergoing lattice restructuring and shrinking to a record-small size of 2 nm, which is the smallest reported for Bi/C composites as far as we know. The Bi nanocrystals are uniformly anchored onto rGO nanosheets by strong Bi—O—C bonds, which not only suppress particle aggregation but also establish efficient ion/electron transport channels and alleviate volume expansion during lithiation. As a result, the Bi-rGO-2 anode consisting of 2 nm Bi nanocrystals has an exceptional reversible capacity of 586.7 mAh g^{-1} over 500 cycles under a current density of 100 mA·g^{-1}, nearly doubling that of a Bulk Bi/rGO composite anode (318 mAh·g^{-1}). Theoretical calculations confirm a higher binding energy between Bi and rGO at small particle sizes, while kinetic analysis reveals accelerated Li^+ diffusion. This work provides a scalable way to design high-performance alloy anodes through metastable nanocrystal engineering and covalent interface coupling.

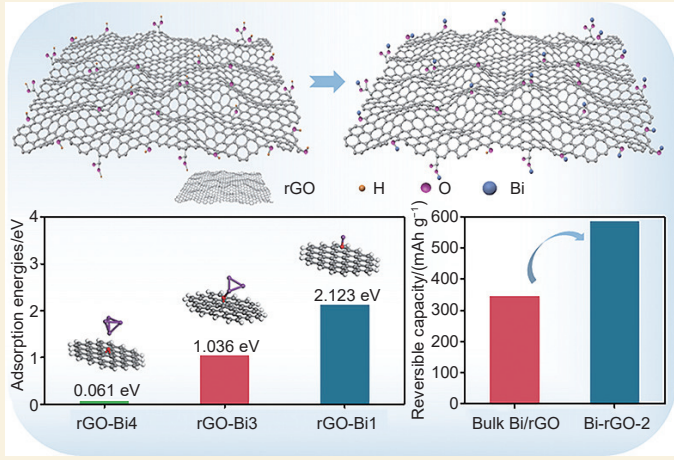

Key words: Laser irradiation technology; Metastable Bi nanocrystals; Reduced graphene oxide; Interface compatibility; Lithium storage

1 Introduction

The rapidly escalating demand for electrification of transport and the expansion of grid storage systems has driven unprecedented advancements in lithium-ion battery (LIB) technology, particularly in energy/power density enhancements, thereby accelerating the critical development of high-power and high-capacity electrode materials[1]. The ideal anode materials, which serve as the foundation for achieving the high-power and high-capacity LIBs, should exhibit exceptional capacity, outstanding rate capability, prolonged cycle stability, and an appropriate voltage plateau[2]. Alloy anodes (e.g., Sb, Sn and Bi) have received widespread attention owing to their favorable operating potential, remarkable energy density, and superior electrical conductivity[3]. Bi and Li^+ can form Li_3Bi through an alloying reaction, which

Received: September 26, 2025
Revised: December 04, 2025
Accepted: December 04, 2025

can obtain a mass-specific capacity of 385 mAh g^{-1} or a volume-specific capacity of 3800 mAh cm^{-3}, becoming one of the ideal anode materials for LIBs[4]. Not only that, Bi also has a high redox reaction potential (0.5–0.75 V), which is conducive to inhibiting the dendrite formation and maintaining the safety of the batteries during charging and discharging, making it an ideal candidate for high-energy-density battery anodes[5]. Notwithstanding, like most known metal-based anodes, large volume expansion (215%) of Bi-based anodes can undesirably cause the pulverization of electrode material during the alloying and dealloying processes, which in turn results in a rapid capacity decay[6–7]. Additionally, the relatively low ion diffusion coefficient of Bi restricts the capacity and cycling performance of LIBs[8].

Various strategies have been attempted to solve these puzzles, such as controlling the size to nanometer level[9], combining Bi with other elements[10–11], and surface modification of Bi anodes[12]. Anchoring Bi particles on carbonaceous materials by stronger interactions has been validated as an effective strategy to buffer mechanical stress and alleviate volume expansion during the Li^+ intercalation process while improving the transport capabilities of ions and electrons[13–14]. For example, Li et al.[15] enhanced the electron transport by employing Bi nanoparticles supported on N-doped porous carbon by a facile replacement reaction method. Yang et al.[16] demonstrated that Bi nanoparticles were anchored onto graphene layers through a laser-induced compositing approach, illustrating an electrode cyclability enhancement mechanism. Nover theless, the cycling capacity and rate performance of the battery are still limited due to the incomplete interface contact caused by the large particle size. Further reducing the size of Bi nanoparticles can further enhance interface contact as well as shorten ion diffusion distance and expose more active Li^+ storage sites, while alleviating volume expansion, showing more excellent electrochemical performance[17–18]. For example, Shi et al.[6] synthesized fibrous Bi@C composites incorporating Bi nanoparticles with particle sizes of ~ 100 nm. Those materials delivered a specific capacity of 415.3 mAh g^{-1} at a current density of 100 mA g^{-1} over 100 cycles. Moreover, Yuan et al.[19] prepared densely packed two-dimensional dimpled carbon structures embedded with much finer Bi nanoparticles with a size of ~ 20 nm, exhibiting improved electrochemical performance, offering a higher specific capacity of 523 mAh g^{-1}. Further, Kim et al.[20] fabricated Bi@C nanoplates composed of around 10–50 nm Bi nanoparticles, which delivered a specific capacity of 556 mAh g^{-1} at a current density of 100 mA g^{-1} over 100 cycles. However, due to the limitations of traditional synthesis methods, smaller nanoparticles often suffer from severe particle aggregation caused by high surface energy, and the smallest reported size limoitation of Bi particles is 5 nm[15]. Thus, the significant technical bottleneck is the preparation of ultrafine and monodispersed Bi nanoparticles. It is highly desirable but quite challenging to develop a controllable strategy for preparing Bi nanoparticles, as well as anchored Bi nanoparticles on carbonaceous substrates in pushing Bi-based anode materials toward practicality.

Herein, we propose an easy strategy for laser manufacturing of metastable Bi nanocrystals in liquid, followed by a solvothermal reaction with graphene oxide (GO), forming Bi and rGO composite (Bi-rGO) anode (Fig. 1a). The diameter of Bi nanocrystals shrinks from 5.5 to 2 nm due to the changes of the internal lattice structure of metastable Bi nanocrystals under high temperature and pressure, resulting in an increase in the interaction force between them and ethylene glycol, leading to volume shrinkage, which is a breakthrough of Bi particles size in Bi/C composite materials as far as we know. Moreover, uniformly dispersed Bi nanocrystals are tightly immobilized on the rGO nanosheets by strong chemical bonds (Bi—O—C), providing interface transport channels for ions/electrons, effectively mitigating the volume expansion of Bi during alloying. Benefiting from the afore-mentioned superiority, the Bi and rGO composite anode delivers a reversible capacity of 586.7 mAh g^{-1} at 100 mA g^{-1} after 500 cycles, which is higher than that of the bulk Bi and rGO composite anode (318 mAh g^{-1}) and exceeds the reported Bi/C anodes

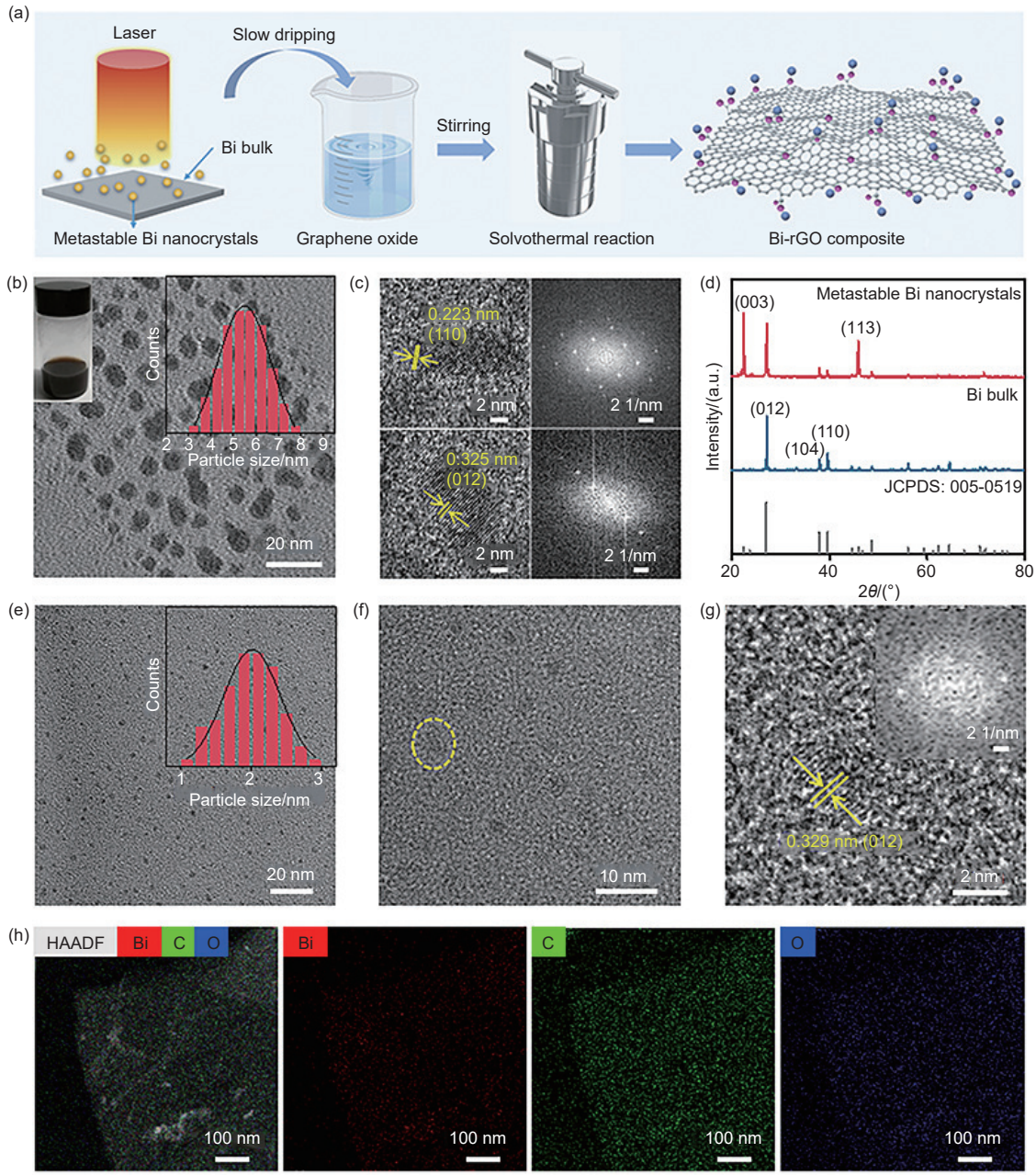

Fig. 1 (a) Schematic diagram of the preparation process of Bi-rGO composite. (b) TEM image. (c) The high-resolution TEM images and the corresponding SAED patterns of metastable Bi nanocrystals. (d) XRD patterns of the Bi bulk and metastable Bi nanocrystals. (e) TEM image. (f) The high-resolution TEM image and (g) The enlarged image of circle from Fig. 1(f) of Bi-rGO-2. (h) HAADF image and EDS images of Bi element, O element and C element. The insets in Fig. 1(b) are the digital photo and the size distribution histogram of metastable Bi nanocrystals suspension after irradiation. The inset in Fig. 1(e) is the size distribution histogram of Bi nanocrystals in Bi-rGO-2

for Li^+ storage. Our strategy can guide the structural adjustment of future Bi-based anodes to achieve wider application.

2 Experimental

2.1 Material preparation

Bismuth (Bi, 99.99%) bulk and powders were purchased from Zhong Nuo Advanced Material (Beijing) Co. Ltd. Ethylene glycol (EG, 98%) was bought from Shanghai Macklin Biochemical Technology Co. Ltd. Graphene oxide (GO, 0.5–5 μm, 0.8–1.2 nm) was procured from Nanjing XFNANO Materials Tech Co. Ltd. Polyvinylidene difluoride (PVDF, 99.99%) and N-methyl pyrrolidone (NMP, 99.9%) were supplied by dodochem.com. Conductive carbon black (Super P, 98.8%) supplied by Hefei Kejing Ma-

terial Technology Co. Ltd., was subjected to vacuum drying at 80 °C for 24 h before use.

2.2 Synthesis of metastable Bi nanocrystals

The bulk Bi was put in a bottle (20 mL) with EG (5 mL), and then the mixture was exposed to the pulse laser irradiation for 60 s. The irradiation employed an Nd: YAG laser (1064 nm wavelength) with a pulse width of 10 ns, a repetition frequency of 10 Hz, and a laser fluence of 973 mJ pulse^{-1} cm^{-2}. All irradiated Bi nanocrystal dispersion was collected. During the irradiation process, ultrasonication was consistently used for the uniform dispersion, and N_2 gas was supplied to prevent oxidation.

2.3 Synthesis of Bi-rGO composite

The Bi-rGO composites were fabricated through a solvothermal reaction, followed by freeze-drying. Specifically, the as-prepared Bi nanocrystal dispersion was gradually introduced through dropwise addition into a pre-sonicated GO suspension (1 mg mL^{-1}) under vigorous magnetic stirring to ensure homogeneous phase integration. Subsequently, the mixture was placed into a high-pressure reactor, where it was maintained at 180 °C for 6 h. Following natural cooling to room temperature, the as-obtained mixture divided into two layers, the supernatant was sucked out and the precipitates were collected, and then the product was washed three times with deionized water to remove residual EG. Finally, freeze-drying was performed to obtain composite materials. To adjust the loading number of Bi nanocrystals, GO was fixed at 50 mg, and the volume of Bi nanocrystal dispersion was changed to 150, 300 and 450 mL. The result is that the Bi nanocrystal content was 50.0%, 69.4% and 77.2% (mass fraction), and the corresponding composite was named as Bi-rGO-1, Bi-rGO-2 and Bi-rGO-3, respectively. Micrometer-sized Bi particles were used for solvothermal reaction according to the above procedure for comparision purposes, and the resulting composite material was named Bulk Bi-rGO. The composite material obtained by directly physically mixing micrometer-sized Bi particles with solvothermal reduced GO was defined as Bulk Bi/rGO.

2.4 Material characterization

The morphological and compositional characteristics of the Bi nanocrystals and their composites were characterized using field-emission scanning electron microscopy (FE-SEM, NovaTM Nano SEM450) and field-emission high-resolution transmission electron microscopy (FE-HRTEM, Talos F200X), and the latter was equipped with energy-dispersive X-ray spectroscopy (EDS). Chemical states were analyzed by X-ray photoelectron spectroscopy (XPS) on a Kratos Axis Supra instrument with an Al *K*α X-ray source. Crystallographic structures were examined via X-ray diffraction (XRD, X'Pert PRO) with Cu-Kα radiation, scanning 2θ angles from 10° to 90°. Thermal stability was assessed by thermogravimetric analysis (TGA, METTLER) under an argon atmosphere, with samples heated from room temperature to 800 °C at a rate of 10 °C min^{-1}.

2.5 Electrochemical measurements

The lithium-ion storage performances were assessed using CR2025 coin-type half-cells, which were assembled in an argon-filled glove box. To prepare the working electrode, a homogeneous slurry was formed by mixing the active materials, Super P conductive carbon, and PVDF binder in a mass ratio of 7∶2∶1, using NMP as the solvent. The slurry was then uniformly coated onto a copper foil collector and vacuum-dried at 80 °C for 12 h. The resulting electrode film was cut into disks with a diameter of 10 mm, yielding an average active mass loading of approximately 2 mg cm^{-2}. The half-cells were constructed employing lithium metal foil as the counter electrode and a Celgard 2400 membrane as the separator. The liquid electrolyte consisted of 1.0 mol L^{-1} $LiPF_6$ in a mixture of ethylene carbonate (EC) and diethyl carbonate (DEC) (1∶1 by volume), with the addition of 10% (mass fraction) fluoroethylene carbonate (FEC).

Cyclic voltammetry (CV) tests were performed within a voltage window of 0.01–3.0 V, and electrochemical impedance spectroscopy (EIS) measurements were conducted over a frequency range of 100 kHz to 0.1 Hz, using a Bio-Logic electrochemical workstation. Galvanostatic charge/discharge tests and galvanostatic intermittent titration technique

(GITT) measurements at various current densities were carried out on a Land CT2001A battery test system. The GITT protocol involved applying a current pulse of 50 mA g^{-1} for 30 min, followed by a relaxation period of 90 min.

2.6 Computational method and details

All density functional theory (DFT) computations were carried out with the Vienna Ab initio Simulation Package (VASP)[21]. The rGO structure was represented as a slab within a periodic lattice, incorporating a 30 Å vacuum layer introduced along the z-direction to eliminate interlayer interactions. Edge sites of the amorphous rGO structure were passivated with hydrogen atoms to ensure structural stability. The Perdew-Burke-Ernzerhof (PBE) generalized gradient approximation (GGA) was adopted to describe exchange–correlation effects. A plane-wave cutoff energy of 400 eV was applied throughout the Calculations. Sampling of the Brillouin zone was performed using a gamma-centered 1×1×1 k-point mesh.

During the calculation process, convergence thresholds were set to 1×10^{-5} eV/atom for energy and 0.02 eV/Å for forces. The adsorption energy (E_{ad}) was calculated as $E_{ad}=E_{slab+X}-E_{slab}-E_X$, where E_{slab+X}, E_{slab}, and E_X correspond to the total energy of the adsorbed system, the clean slab, and the isolated adsorbate X, respectively.

3 Results and discussion

3.1 Morphology and structural analysis of metastable Bi nanocrystals

The metastable Bi nanocrystals were synthesized through a one-step liquid-phase method employing pulsed laser irradiation (Fig. 1a)[22]. Specifically, the bulk Bi was put into a bottle containing EG and pulsed laser irradiation (wavelength: 1064 nm) under room temperature and pressure. After laser irradiation for 60 s, the solution changes from colorless to dark brown (Fig. S1a). This color change results from the laser bombardment exfoliating the bulk Bi, producing numerous uniformly distributed Bi nanocrystals (Fig. 1b and Fig. S1b). The particle size distribution histogram (inset, Fig. 1b) indicates an average nanocrystal size of 5.5 nm. High-resolution TEM images (Fig. 1c) reveal interplanar spacings of 0.223 and 0.325 nm, which correspond to the d-spacings of the (110) and (012) crystallographic planes of Bi (JCPDS: 005-0519)[23].

To identify the crystallinity of metastable Bi nanocrystals, the laser irradiation dispersion liquid was placed on a single-crystal silicon, and EG was evaporated at 150 °C for XRD measuring (Fig. 1d). It can be observed that the characteristic peaks of original bulk Bi were located at 27.3°, 38.0° and 39.7°, corresponding to the (012), (104) and (110) planes of Bi crystal (JCPDS: 005-0519), respectively[24]. The characteristic peaks of Bi nanocrystals also appeared at the same positions after laser irradiation, but the intensity of characteristic peaks at 22.5° and 46.0° is enhanced due to the increased exposure of (003) and (113) planes compared with the original Bi bulk, indicating that laser irradiation does not cause changes in crystal properties[24]. Taken together, metastable Bi nanocrystals have been successfully synthesized, while preserving their crystal structure and chemical composition. These nanocrystals are anticipated to form composites with carbon substrates, as demonstrated below.

3.2 Preparation and analysis of Bi-rGO composite

The above metastable Bi nanocrystal dispersion is evenly mixed with the GO dispersion in EG, followed by a solvothermal reaction, which was designated as Bi-rGO[25]. From Fig. S2**,** it was found that rGO has an irregular multi-layer sheet-like structure, and Bi nanocrystals are embedded in the rGO. Moreover, a large number of Bi nanocrystals show a monodisperse state, uniformly distributed on the rGO substrate (Fig. 1e), and the diameter size of Bi nanocrystals shrinks from 5.5 to 2 nm (the inset of Fig. 1e), which is currently the reported smallest size of Bi particles in Bi/C composite anode materials (Fig. S3 and Table S1). This may be attributed to the changes in the internal lattice structure of metastable Bi nanocrystals under high-temperature and high-pressure conditions, which enhances the interaction force between them and ethylene glycol, consequently indu-

cing volume shrinkage[26]. Of note, the ultrafine and well-dispersed Bi nanocrystals inside carbon can shorten the ions/electrons diffusion distance, while guaranteeing a full utilization of active materials[27]. The high-resolution TEM images of Bi-rGO and corresponding electron diffraction patterns show clear boundaries at the interface between Bi nanocrystals and amorphous carbon. An interplanar spacing of 0.329 nm is observed, which matches the (012) plane of Bi crystals (JCPDS: 005-0519)[23], as shown in Fig. 1f-g. The dark-field scanning TEM and corresponding elemental mapping images illustrate the inlaying of Bi nanocrystals within rGO and the uniform distribution of Bi nanocrystals along the carbon skeleton (Fig. 1h and Fig. S4). Fine-sized and uniformly distributed Bi nanocrystals can shorten the ion transport path and alleviate volume expansion during alloying, which enhances the cycling stability[17].

The Bi content in Bi-rGO composite was determined by TGA, which was 50.0% (Bi-rGO-1), 69.4% (Bi-rGO-2) and 77.2% (Bi-rGO-3), respectively (Fig. 2a). To identify the phase and crystalline characteristic, XRD analysis was conducted[25]. From Fig. 2b, it can be observed that the diffraction peaks of Bi-rGO-1, Bi-rGO-2 and Bi-rGO-3 can be indexed to the Bi metals (JCPDS: 005-0519), but the diffraction peak of rGO was unfound[6]. To verify that GO has undergone a reduction reaction, the GO dispersion without Bi nanocrystals was subjected to solvent-thermal reaction under the same conditions, and the obtained samples show that the diffraction peaks shift to higher angles. This is a typical characteristic of the reduction of GO, indicating that GO has undergone a reduction reaction (Fig. S5)[28].

The bonding structure of Bi-rGO was examined by XPS (Fig. 2c-f). The Bi 4f spectra are deconvoluted into Bi $4f_{7/2}$ (metal), Bi $4f_{7/2}$ (Bi—O), Bi $4f_{5/2}$ (metal), and Bi $4f_{5/2}$ (Bi—O)[29]. The Bi—O bonds come from Bi—O—C bonds formed at the interface between Bi and the rGO. It can be seen that at a Bi content of 50.0%, the main peak area for Bi—O bonds is 96.3%, while that for metallic Bi is 3.7%, indicating that the Bi nanocrystals are fully bonded with rGO. When the content increases to 69.4%, the Bi—O

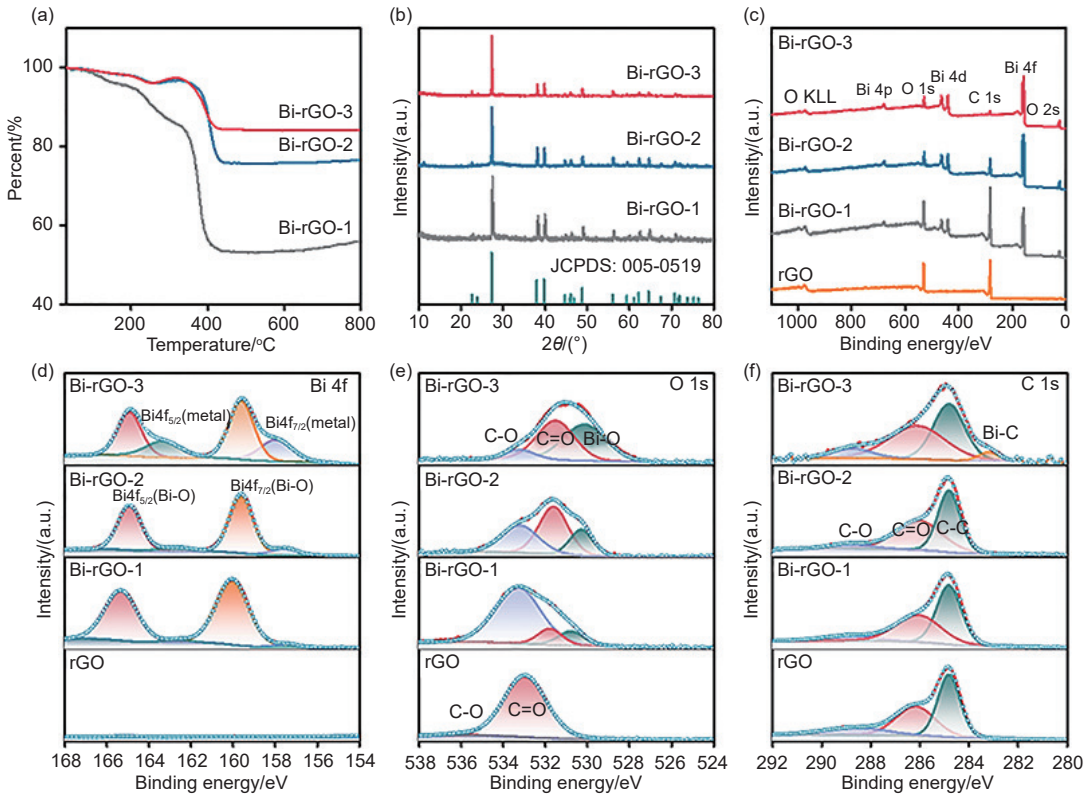

Fig. 2 (a) TGA curves of Bi-rGO composite with different Bi nanocrystals contents. (b) XRD patterns of Bi-rGO with different Bi nanocrystals contents. (c) Survey spectra and high-resolution XPS spectra of (d) Bi 4f, (e) O 1s and (f) C 1s of Bi-rGO composite with different Bi nanocrystals contents

bond peak area decreases to 87.8% and the metallic Bi peak area rises to 12.2%. Further increasing the content to 77.2% results in a significant decrease in the Bi—O bond peak area to 66.2% and a corresponding increase in the metallic Bi peak area to 33.8%. This suggests that when excess Bi nanocrystals are added, a greater portion may not form bonds with rGO[19]. What's more, as the Bi nanocrystal content increases, the peaks of Bi—O bonds shift towards low binding energy, indicating the formation of more Bi—O bonds between Bi nanocrystals and rGO. From the O 1s high-resolution XPS spectra (Fig. 2e), it can be observed that there is an additional peak of Bi—O bond at around 531.6 eV after the addition of Bi nanocrystals[30]. With the increase of Bi nanocrystal content, the peaks of C—O, C=O and Bi—O shift towards low binding energy, further confirming the successful bonding between Bi nanocrystals and rGO. From the C 1s high-resolution XPS spectra (Fig. 2f), it can be observed that Bi-rGO-3 shows a small amount of Bi—C bonds as the Bi nanocrystal content increases, indicating an excess of Bi nanocrystals[31]. As can be seen from the above, the Bi nanocrystals are covalently coupled with rGO through Bi—O—C bonds. When there is an excess of Bi nanocrystals, part of the Bi nanocrystals exist independently and a small amount of Bi—C bonds are formed[32]. Furthermore, SEM characterization reveals the morphology and structure of the Bi-rGO composite (Fig. S6). Initially, the composite becomes increasingly porous with increasing Bi content to 69.4%. However, severe agglomeration occurs at 77.2%, which is likely to hinder ion insertion and extraction during cycling. This morphological evolution impacts performance because the electrochemical properties of electrode materials are closely linked to their morphology and structure[33].

3.3 Electrochemical performance of Bi-rGO composite

The successfully prepared Bi-rGO composite as LIBs anode was characterized by the Li^+ ion storage performance[34]. Fig. 3a compares the cycling stability performance of the different Bi-rGO electrodes at a current density of 100 mA g^{-1}. The Bi-rGO-2 electrode delivered an initial reversible capacity of 677.5 mAh g^{-1} at 50 mA g^{-1}, with a Coulombic efficiency of 65.9% (Fig. 3b). Comparatively, Bi-rGO-1 and Bi-rGO-3 exhibited close initial reversible capacities of 576.7 and 589.2 mAh g^{-1}, with Coulombic efficiencies of 66.4% and 66.0%, respectively (Fig. S7). The initial capacity loss is primarily due to the formation of a solid electrolyte interphase (SEI), originating from the decomposition of the electrolyte and other irreversible side reactions[35]. After the initial 50 cycles, a gradual capacity rise occurs, attributed to SEI stabilization, which reduces lithium loss and activates more lithium-ion storage sites. After 500 cycles, Bi-rGO-2 maintained a superior reversible capacity of 586.7 mAh g^{-1}, outperforming other reported Bi/C electrode materials (Fig. 3c and Table S2). Pronounced fluctuations beyond 400 cycles likely originate from repeated cracking and reformation of the SEI film, caused by volume changes in bismuth nanocrystals during cycling, leading to inconsistent lithium (de)insertion and efficiency variation. To verify the rate performance, the charge and discharge tests were conducted at different current densities from 100 to 2000 mA g^{-1} (Fig. 3d). At the current densities of 100, 200, 500, 1000 and 2000 mA g^{-1}, Bi-rGO-2 show the reversible capacities of 570.8, 446.4, 295.3, 223.3 and 159.9 mAh g^{-1}, respectively (Fig. 3e). When the current density gradually recovers to 100 mA g^{-1}, the reversible capacity reaches 327.1 mAh g^{-1}, superior to that of Bi-rGO-1 and Bi-rGO-3 (Fig. S8). Generally, the reversible capacity should increase with the increase of Bi nanocrystal content due to a higher capacity of Bi. However, in experiments, the reversible capacity first increases, followed by a decrease, as the Bi nanocrystal content increases. This may be due to the excessive addition of Bi nanocrystals, leading to severe aggregation of composite material, blocking its active reaction sites, and deteriorating the microstructure conductivity[36]. Therefore, an appropriate content of Bi nanocrystals can increase the capacity while fully utilizing the conductivity of rGO[17]. With the above-optimized conditions, 69.4% (mass fraction) of Bi nanocrystal content is selected as the optimized

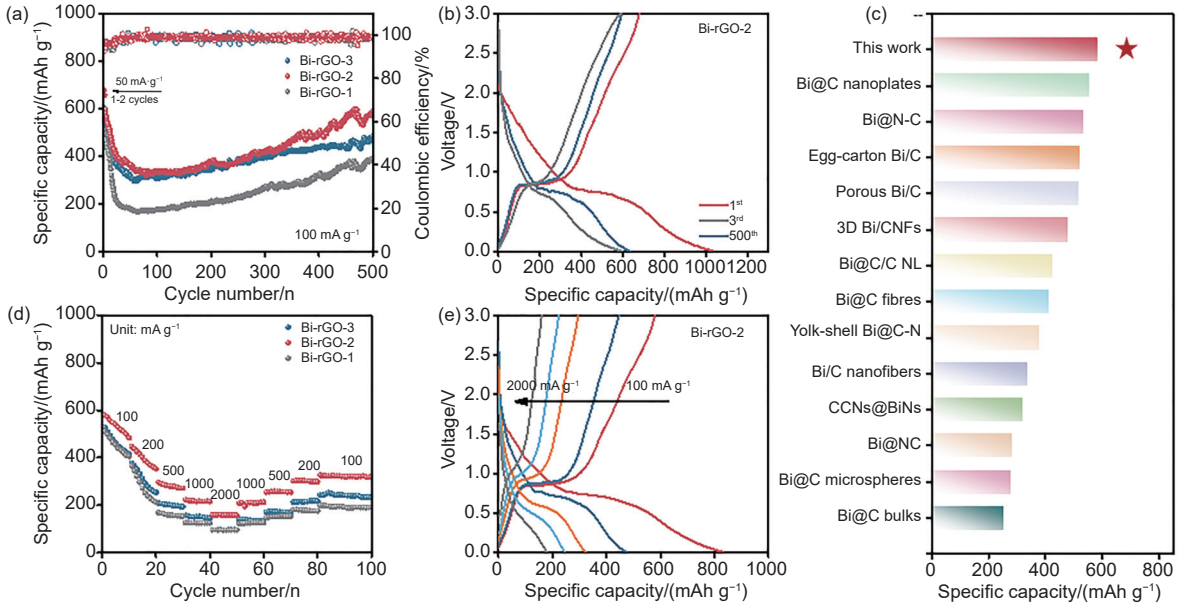

Fig. 3　(a) Cycling performances of Bi-rGO composites and (b) the corresponding discharge-charge curves of Bi-rGO-2. (c) The electrochemical properties of reported Bi-based anodes for LIBs, corresponding Table S2. (d) Rate performances of Bi-rGO composites and (e) The corresponding discharge-charge curves of Bi-rGO-2

amount in the subsequent study.

To demonstrate the superior properties of laser-irradiated Bi nanocrystals for composite anode materials, systematic computational studies were carried out by density functional theory, utilizing the Vienna Ab Initio Simulation Package[37]. The results reveal that the binding energy between Bi and rGO increases with decreasing Bi size, suggesting the enhanced reactivity (Fig. 4a)[38]. To furtherly demonstrate the size effect of Bi particles, micrometer-sized Bi particles were used by directly solvothermal reaction for forming Bulk Bi-rGO (Fig. S9). However, the loading amount of Bi particles is only 35.5%, much lower than Bi-rGO-2. It may be due to the limited contact area between Bi particles and GO, which limits the reaction progress (Fig. S10). At a current density of 50 mA g^{-1}, the initial reversible capacity of Bulk Bi-rGO is 580.9 mAh g^{-1}, and the reversible capacity is 404.4 mAh g^{-1} after 500 cycles (Fig. S11), which is much lower than that of Bi-rGO-2 (586.7 mAh g^{-1}). This is because the ultrafine-sized Bi nanocrystals of Bi-rGO expose more active reaction sites, and their high loading capacity provides higher capacity. Meanwhile, the Bulk Bi-rGO anode was evaluated for its rate performance across various current densities. The corresponding discharge-charge curves indicate that the platform voltage decreases at a current density of 500 mA g^{-1} (Fig. S12). Inconsistent voltage platforms indicate poor electrochemical stability[15].

To eliminate the influence of Bi particle content, a certain number of Bi particles was directly mixed with rGO to obtain Bulk Bi/rGO. The characterization results show that the loading amount of Bi particles in Bulk Bi/rGO is 69.9% (Fig. S13), which is close to Bi-rGO-2 (69.4%). At a current density of 50 mA g^{-1}, Bulk Bi/rGO exhibits an initial reversible capacity of 584.5 mAh g^{-1}, but it only retains a reversible capacity of 318 mAh g^{-1} after 500 cycles at a current density of 100 mA g^{-1}, lower than that of Bi-rGO-2 (Fig. 4b and Fig. S14). Moreover, at a high current density of 500 mA g^{-1}, Bi-rGO-2 also shows higher capacity and cycling stability (Fig. 4c). This is due to the ultrafine size of Bi nanocrystals and the Bi—O—C bond formed with rGO, which shortens the Li^+ ion transport path and slows down the volume expansion during alloying, maintaining structure integrity. To further explore the structure-performance correlation, the thickness changes of the electrode cross-section were analyzed by SEM after lithiation and delithiation in the initial cycle (Fig. 4d)[19]. The thickness of Bi-rGO-2 electrodes is 27.5 μm before lithiation and 30 μm after lithiation, with a change ratio of

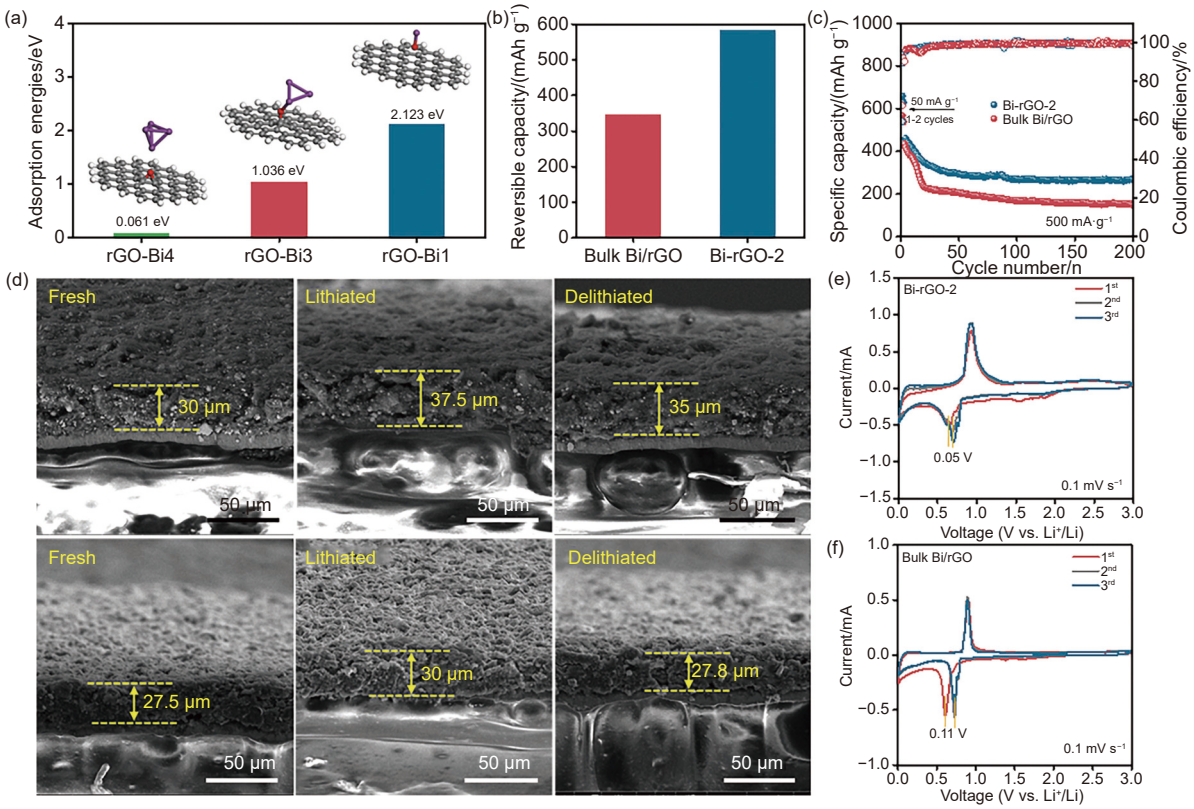

Fig. 4 (a) The adsorption energy between rGO and difference size of Bi. (b) Compared of reversible capacities of Bi-rGO-2 and Bulk Bi/rGO anodes at the current density of 100 mA g^{-1} after 500 cycles. (c) Cycling performances of Bi-rGO-2 and Bulk Bi/rGO anodes at a current density of 500 mA g^{-1}. (d) Cross-sectional SEM images of Bi-rGO-2 and Bulk Bi/rGO anodes before and after lithiated and delithiated. CV curves of (e) Bi-rGO-2 and (f) Bulk Bi/rGO at a scan rate of 0.1 mV s^{-1}

only 9.1%. In contrast, the thickness of Bulk Bi/rGO electrode is 30 μm before lithiation and 37.5 μm after lithiation, with a change ratio of 25%. The thickness variation of the Bi-rGO-2 electrode is significantly lower than the theoretical value of pure Bi (~ 215%)[39]. After delithiation, the thickness of Bi-rGO-2 electrode has recovered to its original thickness (27.8 μm) with a difference of only 0.3 μm, while the thickness of Bulk Bi/rGO electrode is 35 μm with a difference of 5 μm. This indicates that ultrafine Bi nanocrystals were embedded in rGO, alleviating their volume change during lithiation and thus being beneficial for structural stability.

To explore the lithium storage mechanism, CV curve tests were conducted on the Bi-rGO-2 and Bulk Bi/rGO within the voltage range of 0.01 to 3.0 V (Fig. 4e-f). During the first cathodic scan, the irreversible peaks of Bi-rGO-2 at 1.87 and 1.54 V come from the SEI layer formed by electrolyte decomposition, followed by the main reversible reduction peak observed at 0.65 V, and a weak shoulder peak on the right (0.74 V), corresponding to the alloying reaction process of Bi ($Bi+Li^{+}+e^{-}\leftrightarrow LiBi$ and $LiBi+2Li^{+}+2e^{-}\leftrightarrow Li_3Bi$)[4,19]. During the first anodic scan, the sharp oxidation peak at 0.93 V corresponds to the dealloying reaction process of Li_3Bi ($Li_3Bi\leftrightarrow Bi+3Li^{+}+3e^{-}$). In the subsequent two scans, the peak of the cathode shifted towards high voltage, reaching 0.69 and 0.70 V, and the voltage hysteresis was only 0.04 and 0.05 V, respectively, which was lower than most alloy-type anode electrode materials[40]. Moreover, the peak value of Bi-rGO-2 in all 3 scans was at 0.93 V, indicating that it has excellent cycling stability. For comparison, the initial three CV curves of Bulk Bi/rGO electrode were also tested, which show similar electrochemical behaviors with Bi-rGO-2, indicating that their lithiation/delithiation processes are consistent. In addition, Bulk Bi/rGO has similar redox characteristic peaks with Bi-rGO-2 during the first lithiation and delithiation process. The cathode

peak shifted towards high voltage during the last two scanning processes, showing a higher voltage hysteresis (0.11 V), indicating poor cycling stability of Bulk Bi/rGO. This is due to the ultrafine size of Bi nanocrystals, enhanced interface contact and Bi—O—C bonds of Bi-rGO-2 provide more ion transport channels.

In addition to the intrinsic characteristics of electrode materials, the stability of electrode structure is also a critical factor for the process of charging/discharging[35]. Since embedding ultrafine Bi nanocrystals in rGO promotes charge transfer in the Bi-rGO-2 composites, kinetic analysis was performed as shown in Fig. 5. As the scan rate increases, the CV curves of the Bi-rGO-2 and Bulk Bi/rGO electrodes exhibit similar shapes. Both the anodic and cathodic peak currents increase simultaneously with scan rate, which further demonstrates the reversibility of the redox reactions[31]. The relationship between the peak current (I_p) obtained from the CV curve at different scanning rates (v) and the scan rate follows the formula: $I_p=v^b$, where b is an adjustable value that quantifies the relative contributions of capacitive and diffusion-controlled processes to the total current[41]. In general,

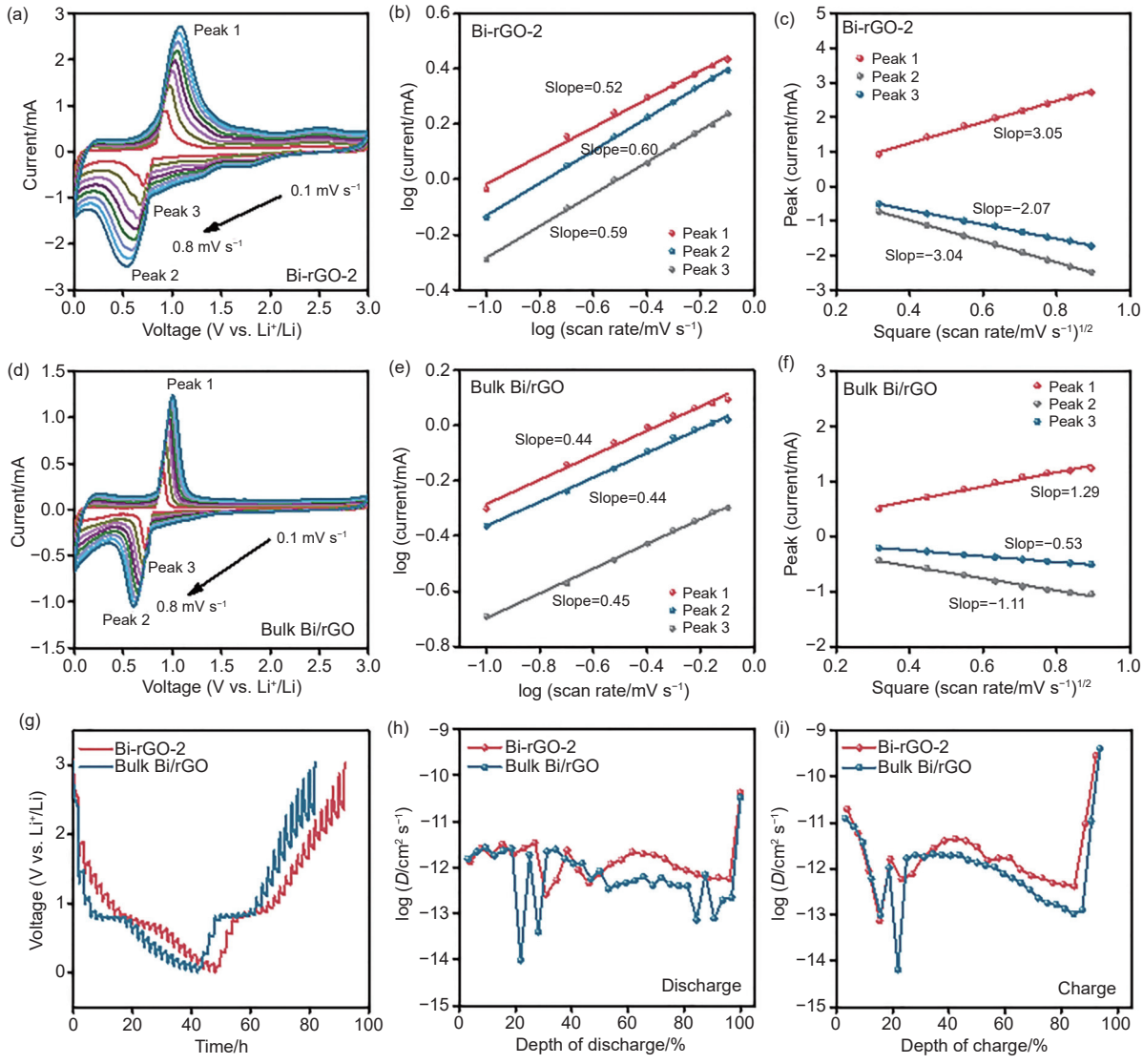

Fig. 5 (a) CV curves of Bi-rGO-2 anode at various scan rates. (b) The relationship diagrams of Log (I_p) and Log(v) of Bi-rGO-2. (c) The relationship diagrams of peak current (I_p) and $v^{1/2}$ for cathodic and anodic peaks derived from the CV curves of Bi-rGO-2 anode. (d) CV curves of Bulk Bi/rGO anode at various scan rates. (e) The relationship diagrams of Log (I_p) and Log(v) of Bulk Bi/rGO anode. (f) The relationship diagrams of peak current (I_p) and $v^{1/2}$ for cathodic and anodic peaks derived from the CV curves of Bulk Bi/rGO anode. (g) The potential response curves of Bi-rGO-2 and Bulk Bi/rGO anodes during GITT measurements. D_{Li} calculated by GITT for (h) discharge and (i) charge processes at 2nd cycle

when a *b*-value of 0.5 signifies a fully diffusion-controlled process, characteristic of reversible Li^+ intercalation, whereas a *b* value of 1, indicates that the total current is completely occupied by capacitive-dominated current. It can be observed that *b* values of the Bi-rGO-2 are 0.52, 0.60 and 0.59, respectively, by linearly fitting peaks 1, 2 and 3 (Fig. 5b), while the *b* values of the Bulk Bi/rGO are 0.44, 0.44 and 0.45, respectively (Fig. 5e). The *b* values of peak 2 and peak 3 are both higher than that of peak 1, indicating that the alloying rate is faster than the dealloying rate. During the oxidation-reduction process, the *b* values of the Bi-rGO-2 are all greater than those of the Bulk Bi/rGO, which is due to the ultrafine-sized Bi nanocrystals in the Bi-rGO-2 shortening ion diffusion distance, and the presence of Bi—O—C bonds accelerates the conduction of ions and electrons, which helps improve conductivity and surface capacitance behavior[31].

The classic Randles-Sevcik formula: $I_p=2.69\times10^5 n^{3/2} A D_{Li}^{1/2} v^{1/2} C_{Li}$, was further utilized, and the diffusion rate of Li^+ of Bi-rGO-2 and Bulk Bi/rGO was compared by linear fitting between I_p and $v^{1/2}$. The results show that the $I_p/v^{1/2}$ values of anode peak and cathode peak in the Bi-rGO-2 are 3.05, −3.04 and −2.07 (Fig. 5c), respectively, which are much higher than those of the Bulk Bi/rGO (1.29, −1.11 and −0.53), indicating that Bi-rGO-2 has a faster Li^+ diffusion rate than Bulk Bi/rGO (Fig. 5f). Moreover, from the EIS curves of the Bi-rGO-2 and Bulk Bi/rGO electrode, it can be observed that the R_{ct} values of both electrodes before CV testing is greater than those after CV testing (Fig. S16). After CV testing at a scan rate of 1.0 mV s^{-1}, the electrochemical impedance spectra are completely overlapped, indicating that the charge transfer kinetics have been improved during cycling and good stability has been maintained during continuous redox processes. The R_{ct} of Bi-rGO-2 before and after CV testing was lower than that of Bulk Bi/rGO, which is owing to the careful design of Bi—O—C bonds at the heterojunction interface can effectively accelerate charge and ion transfer. The ultrafine Bi nanocrystal structure provides a high degree of contact between the electrolyte and the active material, further promoting the rapid transport of ions and electrons, and endowing them with lower electrochemical reaction resistance[42].

The Li^+ diffusion coefficient (D_{Li}) of Bi-rGO-2 and Bulk Bi/rGO was further evaluated using GITT measurements[43]. Based on Fick's second law, the following simplified equation was employed to estimate D_{Li} from the GITT potential profiles:

$$D_{Li}=\frac{4}{\pi\tau}\left(\frac{m_B V_M}{M_B A}\right)^2\left(\frac{\Delta E_S}{\Delta E_\tau}\right)^2$$

where τ is the duration of the current pulse, m_B the mass of active material, V_M the molar volume, M_B the molar mass, and A the electrode surface area. In a single GITT step, ΔE_S denotes the steady-state voltage change, while ΔE_τ represents the total voltage change during the pulse period t. The ratio m_B/V_M can be derived from the density of the electrode material. Generally, a higher D_{Li} reflects faster electrochemical reaction kinetics. As shown in Fig. 5g, the Li^+ diffusion trend in the 2 materials is similar, indicating that the Li^+ diffusion behavior is consistent. During the lithiation and delithiation processes, Bi-rGO-2 provides a higher D_{Li} in the range of 10^{-13} to 10^{-11} cm^2 s^{-1}, indicating ion transfer kinetics of Bi-rGO-2 are faster due to the close contact between Bi nanocrystals and rGO, which makes electron conduction more efficient, and the stable Bi—O—C bond induced increase in surface electron density[40]. EIS curves of Bi-rGO-2 and Bulk Bi/rGO were further analyzed before and after GITT testing (Fig. S17). The R_{ct} of Bi-rGO-2 is lower than that of the Bulk Bi/rGO, and the lower R_{ct} after cycling indicates the improvement in charge transfer kinetics during cycling[44].

4 Conclusion

In summary, this work focuses on the hindered ion/electron transport resulting from the poor interface compatibility between Bi particles and rGO. Metastable Bi nanocrystals were synthesized in EG by liquid-phase pulsed laser irradiation, followed by their implantation into rGO through a solvothermal reaction. This process yielded a series of Bi nanocrystal-

implanted rGO nanocomposites. Remarkably, the diameter size of Bi nanocrystals decreased significantly from 5.5 to 2 nm, which is currently the smallest particle size of Bi particles reported in Bi/C composite materials to the best of our knowledge. The resulting strong interfacial bonding effectively prevents the agglomeration of ultrafine Bi nanocrystals, thereby providing abundant exposed active sites, shortened ion diffusion distances, and highly efficient electron conduction pathways. Concurrently, the uniform distribution of ultrafine Bi nanocrystals on the rGO matrix effectively mitigates volume expansion during the alloying/dealloying processes. Consequently, the LIBs assembled with the Bi-rGO-2 anode demonstrate exceptional cycling stability and structural integrity, delivering a high reversible capacity of 586.7 mAh g^{-1} at a current density of 100 mA g^{-1} after 500 cycles. This superior performance significantly surpasses that of numerous advanced Bi-based anodes and commercial graphite, highlighting the effectiveness of the unique Bi nanocrystal-implanted rGO architecture in addressing the intrinsic limitations of bismuth anodes for future high-performance LIBs.

Acknowledgements

This work was supported by the National Key R&D Program of China (2024YFB4607600, 2025YFE0119700), the National Natural Science Foundation of China (52322203, 52473220), the Fundamental Research Funds for the Central Universities, and the Key Research and Development Program of Xianyang City (L2024-ZDYF-ZDYF-GY-0011).

References

[1] Qiao Y, Zhao H P, Shen Y L, et al. Recycling of graphite anode from spent lithium-ion batteries: Advances and perspectives[J]. EcoMat, 2023, 5(4): e12321.

[2] Lei H, Li J L, Zhang X Y, et al. A review of hard carbon anode: Rational design and advanced characterization in potassium ion batteries[J]. InfoMat, 2022, 4(2): e12272.

[3] Mahmood N, Tang T Y, Hou Y L. Nanostructured anode materials for lithium ion batteries: Progress, challenge and perspective[J]. Advanced Energy Materials, 2016, 6(17): 1600374.

[4] Yin H, Li Q W, Cao M L, et al. Nanosized-bismuth-embedded 1D carbon nanofibers as high-performance anodes for lithium-ion and sodium-ion batteries[J]. Nano Research, 2017, 10(6): 2156-2167.

[5] Zhao M Y, Cheng W D, Wang X, et al. A study on the nanostructural evolution of Bi/C anode materials during their first charge/discharge processes[J]. Materials (Basel), 2024, 17(5): 1140.

[6] Shi C H, Fu H, Nie J J, et al. Bi@C fibre synthesized by electrostatic spinning as high-performance anode material for Li-ion batteries[J]. Ionics, 2022, 28(11): 4977-4987.

[7] Tian Z Y, Wang Y F, Qin X, et al. Porous silicon/carbon composites as anodes for high-performance lithium-ion batteries[J]. New Carbon Materials, 2024, 39(5): 992-1002.

[8] Zhu D H, Zhu H J, Wu H Y, et al. Bismuth anode engineering for tomorrow's batteries: A review of cutting-edge strategies[J]. Energy Storage Materials, 2025, 75: 103978.

[9] Wei Y, Zhang P, Zhou S J, et al. Encapsulating Bi nanoparticles in reduced graphene oxide with strong interfacial bonding toward advanced potassium storage[J]. Small, 2024, 20(30): e2306541.

[10] Wu X F, Li Z J, Feng W C, et al. Insights into electrolyte-induced temporal and spatial evolution of an ultrafast-charging Bi-based anode for sodium-ion batteries[J]. Energy Storage Materials, 2024, 66: 103219.

[11] Jieun H, Jae-Ho P, Kyung Yoon C, et al. One-pot synthesis of Bi-reduced graphene oxide composite using supercritical acetone as anode for Na-ion batteries[J]. Chemical Engineering Journal, 2020, 387: 124111.

[12] Long H L, Wang J, Zhao S Y, et al. Enable the domino-like structural recovering in bismuth anode to achieve fast and durable Na/K storages[J]. Angewandte Chemie International Edition, 2024, 63(29): e202406513.

[13] Xu X, Xu F, Zhang X, et al. Laser-derived interfacial confinement enables planar growth of 2D SnS_2 on graphene for high-flux electron/ion bridging in sodium storage[J]. Nano-Micro Letters, 2022, 14(1): 91.

[14] Chen R T, Zhu Y X, Luo R, et al. A N-doped carbon with encapsulated Fe and Co particles derived from a metal organic framework for use as the anode in lithium-ion batteries[J]. New Carbon Materials, 2025, 40(2): 355-365.

[15] Zhong Y T, Li B, Li S M, et al. Bi nanoparticles anchored in N-doped porous carbon as anode of high energy density lithium ion battery[J]. Nano-Micro Letters, 2018, 10: 56.

[16] Zhu H J, Wang F C, Peng L, et al. Inlaying bismuth nanoparticles on graphene nanosheets by chemical bond for ultralong-lifespan aqueous sodium storage[J]. Angewandte Chemie International Edition, 2022, 62(2): e202212439.

[17] Hong W W, Wang A N, Li L, et al. Bi dots confined by functional carbon as high-performance anode for lithium ion batteries[J]. Advanced Functional Materials, 2020, 31(2): 2000756.

[18] Qian H, Liu Y, Chen H X, et al. Emerging bismuth-based materials: From fundamentals to electrochemical energy storage applications[J]. Energy Storage Materials, 2023, 58: 232-270.

[19] Yuan H C, Jin Y Q, Chen X N, et al. Large-scale fabrication of egg-carton-inspired Bi/C composite toward high volumetric capacity and long-life lithium ion batteries[J]. ACS Sustainable Chemistry & Engineering, 2019, 7(6): 6033-6042.

[20] Kim M K, Kim M S, Park J H, et al. Bi-MOF derived micro/meso-porous Bi@C nanoplates for high performance lithium-ion batteries[J]. Nanoscale, 2020, 12(28): 15214-15221.

[21] Kresse G and Furthmuller J. Efficient iterative schemes for ab initio total-energy calculations using a plane-wave basis set[J]. Physical Review B, 1996, 54(16): 1169.

[22] Su Y X, Xu F, Qiu Y Q, et al. Electrolyte based on laser-generated nano-garnet in poly(ethylene oxide) for solid-state lithium metal batteries[J]. Chemical Engineering Journal, 2022, 443: 136418.

[23] Xu X J, Wang Z S, Zhang D C, et al. Scalable one-pot synthesis of hierarchical Bi@C bulk with superior lithium-ion storage performances[J]. ACS Applied Materials & Interfaces, 2020, 12(46): 51478-51487.

[24] Xu X J, Zhang D C, Wang Z S, et al. Facile synthesis of yolk-shell Bi@C nanospheres with superior Li-ion storage performances[J]. Acta Metallurgica Sinica-English Letters, 2021, 34(3): 347-353.

[25] Su Y, Mu Z, Qiu Y, et al. Embedding of laser generated TiO_2 in poly(ethylene oxide) with boosted Li^+ conduction for solid-state lithium metal batteries[J]. ACS Applied Materials & Interfaces, 2023, 15(48): 55713-55722.

[26] Song R, Feng S H, Wang H J, et al. Effect of organic solvents on particle size of Mn_3O_4 nanoparticles synthesized by a solvothermal method[J]. Journal of Solid State Chemistry, 2013, 202: 57-60.

[27] Cui R C, Zhou H Y, Li J C, et al. Ball-cactus-like Bi embedded in N-riched carbon nanonetworks enables the best potassium storage performance[J]. Advanced Functional Materials, 2021, 31(33): 2103067.

[28] Deng Z, Liu T T, Chen T, et al. Enhanced electrochemical performances of Bi_2O_3/rGO nanocomposite through chemical bonding as anode materials for lithium ion batteries[J]. ACS Applied Materials & Interfaces, 2017, 9(14): 12469-12477.

[29] Hong W W, Ge P, Jiang Y L, et al. Yolk-shell-structured bismuth@N-doped carbon anode for lithium-ion battery with high volumetric capacity[J]. ACS Applied Materials & Interfaces, 2019, 11(11): 10829-10840.

[30] Liu L, Li S, Hu L, et al. Bi@C nanosphere anode with Na^+-ether-solvent cointercalation behavior to achieve fast sodium storage under extreme low temperatures[J]. Carbon Energy, 2024, 6(9): e531.

[31] Jin Y Q, Yuan H C, Lan J L, et al. Bio-inspired spider-web-like membranes with a hierarchical structure for high performance lithium/sodium ion battery electrodes: The case of 3d freestanding and binder-free bismuth/CNF anodes[J]. Nanoscale, 2017, 9(35): 13298-13304.

[32] Chen Z, Wu Y, Liu X, et al. Bi/Bi_3Se_4 nanoparticles embedded in hollow porous carbon nanorod: High rate capability material for potassium-ion batteries[J]. Journal of Energy Chemistry, 2023, 81: 462-471.

[33] Huang W C, Zhu J, Wang M K, et al. Emerging mono-elemental bismuth nanostructures: Controlled synthesis and their versatile applications[J]. Advanced Functional Materials, 2021, 31(10): 2007584.

[34] Qiu Y, Su Y, Jing X, et al. Rapid closed pore regulation of biomass-derived hard carbons based on flash joule heating for enhanced sodium ion storage[J]. Advanced Functional Materials, 2025, 35(29): 2423559.

[35] Lan J L, Jin Y Q, Qin C J, et al. Bio-inspired rose-like Bi@nitrogen-enriched carbon towards high-performance lithium-ion batteries[J]. Chemistry Select, 2017, 2(24): 7178-7184.

[36] Han X P, Li X, Zhang Y M, et al. Bridging evolution of the solvation sheath to rigid-soft coupling and low-resistance solid electrolyte interface for fast-charging and ultrastable Bi anode[J]. Advanced Functional Materials, 2022, 32(22): 2111074.

[37] Jin C K, Cheng L H, Feng G, et al. Adsorption of transition-metal clusters on graphene and N-doped graphene: A DFT study[J]. Langmuir, 2022, 38(12): 3694-3710.

[38] Hussain R, Saeed M, Mehboob M Y, et al. Density functional theory study of palladium cluster adsorption on a graphene support[J]. RSC Advances, 2020, 10(35): 20595-20607.

[39] Zhang S J, Zhang Y M, Zhang Z Y, et al. Bi works as a Li reservoir for promoting the fast-charging performance of phosphorus anode for Li-ion batteries[J]. Advanced Energy Materials, 2022, 12(19): 2103888.

[40] Liu X H, Xie J, Tang Y K, et al. Bi@C sandwiched carbon nanolayers enables remarkable cyclability at high current density for lithium-ion batteries[J]. Applied Surface Science, 2023, 613: 155996.

[41] Xu X S, Xu F, Qu C Z, et al. Laser-manufactured metastable supranano SnO_x for efficient electron/ion bridging in SnO_2-graphene heterostructure boosting lithium storage[J]. Advanced Functional Materials, 2021, 31(35): 2101059.

[42] Yang F H, Yu F, Zhang Z A, et al. Bismuth nanoparticles embedded in carbon spheres as anode materials for sodium/lithium-ion batteries[J]. Chemistry, 2016, 22(7): 2333-2338.

[43] Xu F, Zhai Y, Zhang E, et al. Ultrastable surface-dominated pseudocapacitive potassium storage enabled by edge-enriched N-doped porous carbon nanosheets[J]. Angewandte Chemie International Edition, 2020, 59(44): 19460-19467.

[44] Long H, Yin X, Wang X, et al.Bismuth nanorods confined in hollow carbon structures for high performance sodium- and potassium-ion batteries[J]. Journal of Energy Chemistry, 2022, 67: 787-796.